Chapter 2

Catalog and data processing

2.1 Foreword

As discussed in the introductory chapter, the Io-Jupiter electro-magnetic interaction gives rise to an auroral footprint on the giant planet. The goal of my thesis is to demonstrate that a methodical analysis of UV images of Jupiter's aurorae can significantly contribute to the understanding of this phenomenon. In order to achieve this goal, some rather technical steps have to be taken before moving into the more interpretative part of the work. For example, prior to any detailed investigation, we need to make an inventory of these images and to compile it into a catalogue together with relevant parameters related to each particular observation.

The basic pieces of information we can extract from these images are 1) the position of a particular structure and 2) its brightness. In the context of planetary astronomy, locating a feature usually consists in determining its longitude and latitude on the planet. As a result, we first need to determine the location of the planetary center and the orientation of the planetary rotation axis on the images. Unfortunately, the Hubble Space Telescope pointing parameters are not known with sufficient accuracy for our purpose. The precision of the guide star catalog is on the order of 1 arcseccond while we require and accuracy around 1 pixel, i.e. 0.025-0.03 arcsecond. Since we cannot use the telemetry information contained in the image headers, I developed techniques to retrieve these parameters with the appropriate accuracy from the images themselves.

As far as the brightness is concerned, it is crucial to isolate the intrinsic auroral emissions from background emissions. These background emissions originate from two sources: the geocoronal emissions from the Earth's upper atmosphere that gen-

STIS Clear	STIS SRF2	ACS F115LP	ACS F125LP
0.0236	0.0006	0.0287	0.0015

Table 2.1: Mean number of counts per second and per pixel caused by geocoronal emissions for the different filters considered in this work. The filters excluding H Lyman-α emissions are far less affected by these emissions than those including this line.

erate a uniform noise on the image and Jupiter's planetary disk emissions. These disk emissions are mainly caused by dayglow emissions and by solar light reflections on the Jovian atmosphere. The geocoronal emissions rarely exceed a few counts per pixel for typical HST exposures and can be easily deduced from the brightness measured on an area located away from the planet.

These tools were developed in such a manner as to be easily used by many. This approach allowed me to be involved in many other studies based on Hubble Space Telescope images. Some of these studies will be simply listed at the end of this chapter while others, more closely related to the satellite footprints, are discussed more thoroughly in the relevant chapter.

2.2 HST Observation Programs

More than two thousand UV images and spectra of Jupiter have been taken with the high resolution cameras (STIS and ACS) on board HST since 1997. Each set of images from the different programs has been processed at the time it was acquired. However, several critical corrections and improvements have been added to the processing pipeline with time. In order to perform efficient statistical or detailed analysis of the Jovian aurora in general and of the Io footprint in particular, we needed a well organized data base taking into account the more recent image processing methods. It has been thus decided to re-download all the images and spectra and to process them with the best available reference files[1]. We also processed them with our own routines in a standardized way in order to produce files readily usable with the IDL software. For example, these routines extract and store independently individual exposures when several of them are recorded into the same source file. Other routines generate series of 10-second exposure time images out of

[1]The reference files are the files describing the different corrections that have to be applied to the raw image. It includes the files related to the dark, the flat field and the geometric correction.

the time-tag event lists.

The database consists of the observations acquired during programs 7308 (Clarke)[2] , 7309 (Gérard), 7769 (Prangé), 8108 (Emrich), 8171 (Clarke), 8657 (Clarke) , 9685 (Elsner) 10140 (Grodent), 10507 (Grodent) and 10862 (Clarke). Table 2.2 provides a list of characteristics of these programs together with a one line summary of their scientific objectives. Apart from proposals 8171, 10140 and 10862 which included some observations specifically dedicated to the Io footprint, the presence of the Io footprint on the images was usually not considered as a primary objective. This is an additional justification for building a complete catalog and database in order to select subsets of images where Io is in an appropriate configuration. It also made it possible for us to determine the previously unexplored configurations of Io relative to the plasma torus, which turned out to be particularly useful when the 10862 observation program was put together.

The Hubble Space Telescope orbits around the Earth in approximately 96 minutes at a mean altitude of ∼600 km. Since Jupiter lies close to the ecliptic plane, HST can point at it only during half an orbit, i.e. for ∼45 minutes. During the remainder of the orbital period, Jupiter is occulted by the Earth. In the present work the term "HST orbit" designates the continuous time period during which Jupiter can be seen from Hubble.

The 10862 program is the largest program ever established to observe Jupiter and Saturn. Within a few months of Spring 2007, HST acquired between twice and three times more images of Jupiter than during the previous 10 years. The Jovian side of the campaign[3] was divided into 3 parts. The first part consisted in acquiring images during one orbit for 20 consecutive days and took place from February 20 to March 11 2007, simultaneously to the New-Horizons probe Jupiter fly-by. The second part also consisted in acquiring images during at least one orbit per day from February 20 to March 11. This second time period was chosen close to opposition, from May 11 to June 11, so that MHD simulations can be used to propagate solar wind conditions measured at Earth up to Jupiter. Moreover, on 6 occasions, Jupiter was observed during two to five orbits on the same day. The third part consisted in 10 orbits spread from March 2 to April 24 and exclusively dedicated to the Io and Ganymede footprints.

[2]The name in the parenthesis is the name of the Principal Investigator (or PI) of the programs.

[3]The 10862 campaign was essentially dedicated to the study of the response of the Jovian and Kronian magnetospheres to the solar wind. Therefore, 879 images of Saturn's aurora have also been acquired.

Proposal ID	PI Name	Number of images	Number of time-tags	Number of spectra
7308	J.T.Clarke	40	6	21
Abstract: WFPC2 and STIS auroral observations concurrent to magnetospheric Galileo observations.				
7309	J.-C. Gérard	2	1	6
Abstract: Search for the signature of the H_2 dayglow in the equatorial regions.				
7769	R. Prangé	34	2	16
Abstract: Spectral and imaging observations of the polar regions giving access to auroral atmospheric parameters.				
8108	C. Emrich	0	0	22
Abstract: High resolution STIS spectral observations.				
8171	J.T.Clarke	19	13	36
Abstract: Spectroscopic and imaging study of the satellite footprints during the Galileo mission.				
8657	J.T.Clarke	190	18	37
Abstract: Study of the solar wind impact on the Jovian magnetosphere concurrent to in situ solar wind measurements during the Cassini fly-by.				
9685	R. Elsner	45	6	0
Abstract: Coordinated HST and Chandra observations of Jupiter in order to determine the origin of the X-ray aurorae.				
10140	D. Grodent	100	0	0
Abstract: Study the possible northern Jovian magnetic field anomaly.				
10507	D. Grodent	71	0	0
Abstract: Study of the diffuse auroral emissions poleward and equatorward of the main oval.				
10862	J.T.Clarke	1619	0	0
Abstract: Study of the influence of the solar wind on Jovian magnetosphere and aurorae during the New Horizon probe fly-by.				

Table 2.2: Description of the executed HST programs considered in this study. Only the UV observations were accounted for. The number of time-tags refers only to imaging time-tags. The spectral time-tags are counted in the spectra column.

Moreover, such a large amount of data also required a catalog gathering at the same time information concerning the observation itself (instrument, filter, etc.) and planetary ephemeris (sub-solar latitude, Io System III longitude, etc.). The next sections describe how the catalog has been built, what are the stored parameters and where they come from. The catalog consists of a structure variable saved in an IDL file. In addition to the IDL file, a descriptive ascii file has been generated for each observation, compiling the parameters considered in our catalog.

2.3 Information sources

All the HST data stored on our file system comes from the Space Telescope European Coordinating Facility (ST-ECF) and from the Space Telescope Science Institute (STScI). The first step consists in building a list of all the relevant observations. Knowing the names of the HST programs, the observation list has been computed with the ST-ECF web site [4]. The main information source about the data itself comes from the *.fits* files headers. These headers collect technical information about the data and the telescope telemetry. When a parameter is both available from the websites and from the *.fits* header, the header was always preferentially used. For example, there was a systematic 1 second difference in the start dates between the *.fits* files and on the websites concerning the WFPC2 observations. As far as the ephemeris are concerned, the information is computed with a FORTRAN code based on libraries from the Navigation and Ancillary Information Facility (NAIF) SPICE system [5]. This program was written by Denis Grodent and has been slightly modified in order to provide the sign of the pitch angle[6]. All the temporal data are calculated for the initial moment of the exposure.

Several catalog fields are links to some relevant files, such as the reduced image file or preview images or movies. Other parameters required additional computing like the estimated position of the satellite footprints. Their location on the planet

[4] http://archive.eso.org/wdb/wdb/hst/science/form

[5] http://naif.jpl.nasa.gov/naif/

[6] In this context, the pitch angle is the apparent angle between Jupiter's projected rotation axis and the celestial north direction. It should not be mixed up with the pitch angle describing the angle of a particle velocity relatively to the magnetic field. This angle in measured counter-clockwise. In order to compute the sign of the pitch, the modified program first computes the vector formed by the cross product of North direction vector with the Earth-Jupiter vector. The sign of the pitch angle is equal to the sign of the dot product of this vector with the Jovian rotation axis.

comes from the longitude of the satellites mapped into the ionosphere with the VIP4 magnetic field model. For Io, the VIT4 model[7] has been used and an approximation of the lead angle has also been taken into account. This estimate comes from a 3rd order Fourier fitting of Infrared lead angle measurements provided by J. E. P. Connerney (personal communication). Given the inaccuracies of the magnetic field models and the existence of poorly constrained lead angles, these parameters do not provide reliable positioning of the satellite footprints but just an indication of their likely locations. The accuracy is on the order of 5° in every direction for Europa and Ganymede. For Io, the error can reach up to 15° in the poorly constrained regions.

The last type of parameter is related to our "in-house" data processing. Since the center of the planet on the image as well as its exact orientation are poorly known from telemetry, limb and band fitting methods have been built in the framework of this study. These parameters are also included in the catalog. Similarly, some parameters issued from eye detection of particular footprint features are also included. Note also that some fields are left empty for later use.

[7]The VIT4 model is an unpublished improved version of the VIP4 model and is used by the courtesy of J. E. P. Connerney. This model is essentially constrained by the IFP latitudes, since the probe field measurements are only used to compute the magnetic field intensity. The northern Io contour provided by this model is closer to the observations than the previous one .

2.4 Field description

Name	Type	Origin	Description
target_name	string	header	target name
target_ra	float	header	sighting right ascension
target_dec	float	header	sighting declination
target_descr	string	web	target description
instr	string	header	instrument
data_set	string	header	data set name
hemisphere	string	calculated	hemisphere ("N" for North, "S" for South)
release_date	string	web	release date
date	string	header	date at the begining of the exposure
expt	float	header	exposure time in seconds
filter	string	header	filter
pi_name	string	header	PI name
prop_id	string	header	proposal ID
sp_vers	string	web	spacecraft version
grating	string	header	grating
asn_id	string	header	not used
asn_type	string	header	not used
number	float	header	number of observations in the dataset
camera	string	header	camera
obs_mode	string	header	observation mode
min_wl	float	header	minimum wavelength
max_wl	float	header	maximum wavelength
dispersion	float	header	Not used
bandwidth	float	header	Not used
cent_wl	float	header	central wavelength
pitch	float	SPICE	pitch angle counted counter-clockwise in degrees
jup_ra	float	SPICE	Jupiter right ascension
jup_dec	float	SPICE	Jupiter declination
incl	float	SPICE	angular position of the north pole
latst	float	SPICE	sub-earth latitude in degrees

Name	Type	Origin	Description
cml	float	SPICE	central meridian longitude in degrees System III
latss	float	SPICE	sub-solar latitude in degrees
lonss	float	SPICE	sub-solar longitude in degrees System III
d	float	SPICE	Earth-Jupiter distance in km
light_time	float	SPICE	Earth-Jupiter light-time in seconds
eq_rad	float	SPICE	Jovian equator radius in arcsec
pol_rad	float	SPICE	Jovian polar radius in arcsec
aurora_param	20 floats		Aurora parameters
aurora_comment	string		comments on the aurora
phase_io	float	SPICE	Io phase angle in degrees
lbd3_io	float	SPICE	System III Io longitude in degrees
io_param	20 floats array		Io footprint parameters
io_param(0)	float	computed	Io centrifugal latitude in degrees
io_param(1)	float	vis. insp.	visibility of the Io footprint (0 for no, 1 for yes and 2 for undetermined and -1 if not filled)
io_param(2)	float	vis. insp.	visibility of the precursor (0 for no, 1 for yes and 2 for undetermined and -1 if not filled)
io_param(3)	float	computed	Io footprint System III longitude
io_param(4)	float	computed	Io footprint phase angle
io_param(5)	float	computed	Io footprint latitude
Io_comment	string		comments on the Io footprint
phase_euro	float	SPICE	Europe phase angle in degrees
lbd3_euro	float	SPICE	Syst. III Europe longitude in degrees
euro_param	12 floats array		Europe footprint parameters
euro_param(3)	float	computed	Europa footprint System III longitude
euro_param(4)	float	computed	Europa footprint phase angle
euro_param(5)	float	computed	Europa footprint latitude
euro_comment	string		comments on the Europe footprint

Name	Type	Origin	Description
phase_gany	float	SPICE	Ganymede phase angle in degrees
lbd3_gany	float	SPICE	Syst. III Ganymede longitude in degrees
gany_param	12 floats array		Ganymede footprint parameters
gany_param(3)	float	computed	Ganymede footprint System III longitude
gany_param(4)	float	computed	Ganymede footprint phase angle
gany_param(5)	float	computed	Ganymede footprint latitude
gany_comment	string		comments on the Ganymede footprint
phase_calli	float	SPICE	Callisto phase angle in degrees
lbd3_calli	float	SPICE	Syst. III Callisto longitude in degrees
calli_param	12 floats array		Callisto footprint parameters
calli_comment	string		comments on the Callisto footprint
rootname	string	header	rootname (unique for each image)
extension	string		extension (ex: _rzd)
preview_link	string		link to the preview
video_link	string		link to the video preview
i_s	string	header	image or spectrum The first letter is "I" for images and "S" for spectra. The next two letters are "UV" for UV and "VI" for visible.
tele_data	10 floats array		telescope data
tele_data(0)	float	header	OM1LVPST detector temperature (for the Landsman 98 blotch correction)
tele_data(1)	float	header	detector orientation (i.e. angle between the north axis and the image y axis) measured counter-clockwise in degrees
tele_data(2)	float	defined	angle per pixel (arcsec/pixel)
tele_data(3)	float	header	x dimension of the reduced image (pixel)
tele_data(4)	float	header	y dimension of the reduced image (pixel)
tele_data(5)	float	defined	x position of the Jovian center on the reduced image (pixel)

Name	Type	Origin	Description
tele_data(6)	float	defined	y position of the Jovian center on the reduced image (pixel)
tele_data(7)	float	computed	x position of the Jovian center on the reduced image (pixel)
tele_data(8)	float	computed	y position of the Jovian center on the reduced image (pixel)
tele_data(9)	float	computed	quality flag for the center computation
tele_data(10)	float	computed	corrected pitch angle (degrees)
tt_start	5 floats array		initial moments of the Good Time Interval
tt_stop	5 floats array		final moments of the Good Time Interval
link	string		link to the reduced image
orb	string	calculated	rootname of the first image of the orbit
comments	string	inspection	comments : It contains the "MISSING FILES"statement if the data are not available.

Table 2.3: List of the parameters available in the catalog.

2.5 Data reduction

The WFPC2 data have not been re-reduced yet, neither have the STIS spectra since none of them have been considered in this study. As far as the STIS images and time-tag sequences are concerned, the original data are coming from the *_x2d.fits* files. The ACS images were reduced with the *Multidrizzle* software. The next paragraphs discuss the relevance of corrections applied additionally to the standard pipeline. For STIS data, homemade procedures have been built according to Space Telescope Science Institute (STScI) reports. Since we were looking for a "state of the art" standardized database, we reviewed all the routines as well as their relevance.

2.5.1 STIS data

The dark current[8] on STIS FUV-MAMA has a mean value $\sim 7\times10^{-6}$ count/s/pixel, which is very low. It can be decomposed into two components. The first one is a uniform and temperature-independent flux of 1.6×10^{-6} count/s/pixel while the second can reach 2×10^{-4} count/s/pixel, is temperature dependent and is localized on the upper left part of the image array. *Landsman* (1998) established that the best monitored detector temperature for estimating the temperature dependence was the OM1LVPST low voltage supply temperature. This temperature is available in the *_spr.fits* engineering file that comes with every observation and is included in the catalog. Nevertheless, since this correction is not accurate and remains below 1 count per pixel for every imaging observation (exposure times $< 150s$), we chose not to correct for this dark current component.

As far as the geometric distortion corrections are concerned, *Walsh et al.* (2001) released an Instrument Science Report (ISR) in 2001 describing the correction method for both the NUV and the FUV MAMA. It is based on a third order polynomial description of the geometric distortion field for each detector. The first STIS pipelines did not complete the geometric correction so that homemade procedures relying on the reported method and set of coefficients have been built and used. In 2004, *Maiz-Apellaniz and Ubeda* (2004) released another ISR establishing that the previous geometric correction was not correct for the NUV-MAMA. According to this report, the way the 2001 polynomial parameters have been derived was erroneous. Consequently the FUV-MAMA set of polynomial coefficients is probably incorrect too. Even if the complete set of geometric coefficients have not been computed yet for the FUV detector, STScI provided a new set of coefficients for correcting the fact that the pixels' surface are not exactly squared but rectangular (the y-scale of the pixels is approximately 1% larger than the x-scale). In order to compare the old but full 2001 correction and the new "rectangle-to-square-only" correction, we processed the same Saturn image with both methods and we tried to determine which method best fits the rings. As the old 2001 parameters gave significantly worse results, we chose to correct only the rectangular aspect of the pixels, as performed in the new STIS pipeline for the *_x2d* images. However, the best geometric correction will only be achievable when the STScI releases an updated set of correction parameters.

[8]The dark current is the signal current that flows in a photodetector when it is placed in total darkness

2.5.2 ACS images

The ACS data are directly coming from the *Multidrizzle* image processing pipeline from the STScI[9]. The subtlety arises from the fact that the total number of counts per second on the geometrically corrected images is erroneously 1.63 time larger than on the non-corrected image. Following the purely geometric correction (i.e. relocating the pixels at their correct place), *Multidrizzle* applies an additional photometrical correction for the pixel area. The pixel area map in use for SBC is the same as for the HRC detector, since they share the same deforming[10] optical path. The problem is that this pixel area map (PAM) is normalized to 0.025 arcsec square while the SBC pixels are 0.03377×0.0301 wide. Consequently, the number of counts is artificially multiplied by the pixel surface ratio. We took this effect into account and corrected the count rates accordingly.

2.6 Determination of the planetary center location and rotation axis orientation

The limited accuracy of the HST guide star catalog and the uncertainty in the start time of the tracking motion prevent us from precisely locating the center of Jupiter on the images just from pointing information. However, the determination of the planetary center is a mandatory step before locating any structure in the images. Additionally, the accurate positioning of the center is crucial for building polar projections of the auroral emissions. Several techniques have been used through the years, from manual positioning of a grid to semi-automatic limb fitting methods. The manual positioning remains the more precise technique because all the useful elements, such as the altitude of auroral arcs above the limb or the relative motion of an auroral feature from one image to another, can be taken into account by the operator. Nevertheless, this technique suffers from two major drawbacks: the subjectivity of the operator and the time these manual manipulations consume. Since the data base tremendously inflated with the 10862 observation campaign, this

[9] *http : //stsdas.stsci.edu/pydrizzle/multidrizzle/*

[10] By deforming it is meant that we cannot use the raw image without straightening the geometry. It does not imply that the optics of the instrument is ill designed. Actually, the optical path is designed to compensate the deformation caused by the spherical aberration of the main mirror. The distortion of the raw image stems from the fact that the focal surface is not perpendicular to the chief ray.

method was seen as impracticable for providing first results in a reasonable amount of time. Another major advantage of an automatic procedure is that the complete dataset can be quasi-immediately reprocessed if needed, which is impossible for manual methods. The limb-fitting method[11] designed by Adem Saglam was first developed for Saturn (*Saglam*, 2004), where the illuminated limb is sharp, and then adapted to Jupiter. The method is based on modeling the edge of the planet with a parametric step function. The operator has to select a rectangle containing a section of the limb free from auroral emissions. Each line (or row) is then fitted with the step function. The limb is computed by fitting the contour ellipse of the planet computed from the ephemeris to all the detected step points. Unfortunately, this technique also depends on the operator subjectivity through the rectangle selection and can sometimes be inaccurate, especially for the non-illuminated limb which can hardly be modeled with a step function. Therefore, we developed an automatic procedure based on the detection of the planetary limb inflection point to compute the planetary center.

A multi-step strategy has often been used in the method described below. This approach has been requested by the huge number of particular or problematic cases on one hand and by the demanded final precision on the other hand. The strategy thus consists in a robust but rather imprecise first step and on a refined and more precise second step. Figure 2.5 summarizes the successive tasks of the limb fitting method.

Should the filter perfectly isolate the H_2 and H UV emissions below 1650 Å, the limb altitude would be related to the UV dayglow emission. However, the planetary disk seen on ACS (and STIS in a lesser extent) FUV images mainly results from the reflected solar continuum in longer wavelengths that is leaking into the detector[12] (*Boffi et al.*, 2008). Consequently, a reasonable assumption is that the limb altitude as detected on the images indeed corresponds to the reflected sunlight limb with an inflection point located at the 1 bar level, corresponding to the 0 km altitude assuming an ellipsoid with an equatorial radius of 71492 km and a polar radius of 66854 km. In order to test this hypothesis, we used ACS images of Saturn acquired with the same filters. Saturn being located approximately twice further from the Sun than Jupiter (9.5 AU instead of 5.2 AU), the entire planetary disk as well as

[11] This method is no longer used for Saturn and has been replaced by a ring fitting method also developed by Adem Saglam.

[12] This effect is called red leak.

	Mean (km)	Std. dev. (km)
Equator	157	215
45°S	11	169
65°N	-74	101

Table 2.4: Mean altitude of the radial light curve inflection points on Saturn measured from the 1-bar level. Since one pixel subtends 180 km, we note that the mean altitude as well as the standard deviation of this altitude are on the same order or lower than the pixel size.

a large portion of the ring system appears on STIS and ACS FUV images. As a consequence, on these images, the planetary center can be computed with an independent method, i.e. by fitting the A, B and C rings in lieu of relying on the planetary limb. Elliptic bands, whose dimensions are deduced from ephemeris and from the detector plate scale, are adjusted to the observed rings. The center of these ellipses provides an excellent estimate of the planetary center, with a mean accuracy of $\sim$1 pixel. We then perform radial scans of the day-side limb and compute the altitude of the inflection point given the center location from the ring fitting (Figure 2.1). The mean altitude of the inflection point is measured at 0°, 45°S and 65°N latitudes on the sunlit side of the planet. In the three cases, the mean altitude is almost within a pixel from the 1 bar level (see Table 2.1). Since the atmospheric composition of both giant planets is similar, it is reasonable to assume that the conclusions drawn about the altitude of the inflection point at Saturn are applicable to Jupiter as well.

2.6.1 Co-adding the exposures

Our purpose is to build a fully automatic procedure to locate as accurately as possible the planetary center on all type of STIS and ACS images. The concept is close to the method developed by Adem Saglam, but brings some useful improvements. The first idea is to increase the signal to noise ratio at the maximum when selecting a limb profile. Since the HST pointing is very stable during an observation orbit[13], we summed all the images from the same orbit and acquired with the same pointing target. This is particularly convenient for the ACS observations, when up to 32

[13]The typical pointing stability drift when two guide stars are used is on the order of 0.01 arcsec per orbit, which is less than the size of 1 pixel (0.024 arcsec for STIS or 0.03 arcsec for ACS).

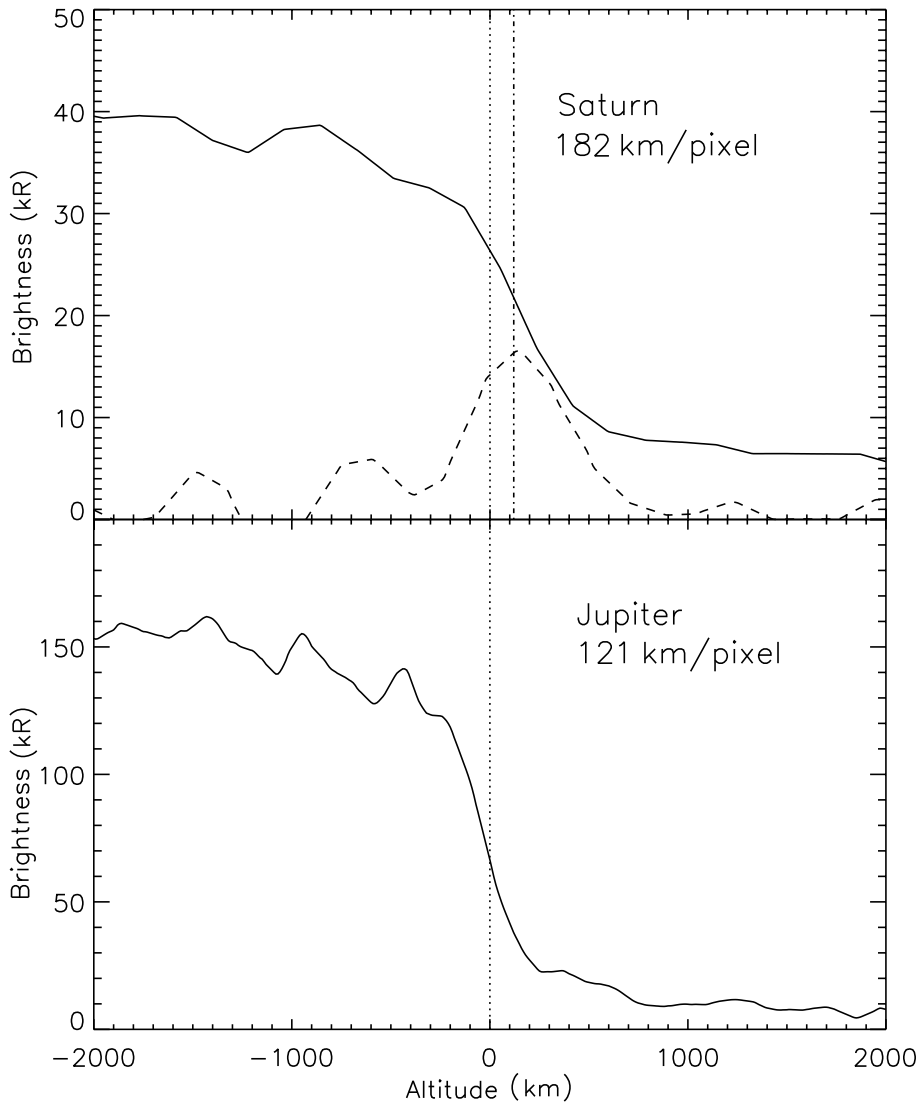

Figure 2.1: Example of an equatorial limb profile at Saturn (a) and at Jupiter (b). The dashed line represents the first derivative of the altitude of the brightness profile. The dotted line represents the 1 bar level, corresponding to 0 km. On Saturn, the altitude of the inflection point (highlighted by the dash-dotted line) is smaller than the pixel size. (from *Bonfond et al.*, 2009)

consecutive images have been acquired within a single orbit. As discussed below, this technique is more complex to apply to images from the 9685 STIS program.

2.6.1.1 Compensation of the inter-image shift for the program 9685

Since the STIS field of view is 25×25 arcsec^2 wide and since Jupiter's apparent diameter is about $\sim$50 arcsec wide, the planet cannot fit entirely into the instrument field of view. Approximately one quarter of the Jovian disk can be seen at a time. As a consequence, the telescope has to be pointed slightly northward from the Jovian center to observe the northern aurora and vice versa for the South. In the other HST/STIS programs, this shift had been calculated by the PI and the pointing position was given in celestial coordinates. However, for the 9685 program, it was requested to track a particular point on Jupiter's surface. The coordinates of this point are 170° in System III longitude and 67.8° in planetographic latitudes[14]. Since this particular point is rotating during an observation sequence, the planetary disk shifts from one image to the other. Consequently, it is necessary to compensate for this additional motion in order to re-align the limbs. Accordingly, a routine was developed in order to calculate the shift of each sub-image from a sequence relative to the first one. It simulates the motion of the point in planetary coordinates and computes the location difference in pixels from one frame to another. This function works for time-tag sequences as well as for sub-images from a same dataset. In Figure 2.2 the left panel represents the superposition of two images from the same dataset without the shift and on the right panel we applied the shift. In the second case, the two planetary disks are perfectly aligned.

2.6.2 Orienting all images consistently

In the following, the word "image" will be used to designate the sum of the exposures. The goal of the automatic limb fitting procedure is to process every image the same way, whatever the orientation of the planetary disk on the detector and whatever the observed hemisphere. Three cases can occur: the disk fills one, two or three corners of the image. In order to detect which configuration should be considered, we need to distinguish the population of points related to the background from the population of points related the planetary disk. This discrimination is performed by using the histogram of the image. In filtered images, there is a clear gap between the

[14]This corresponds to 65° in planetocentric coordinates.

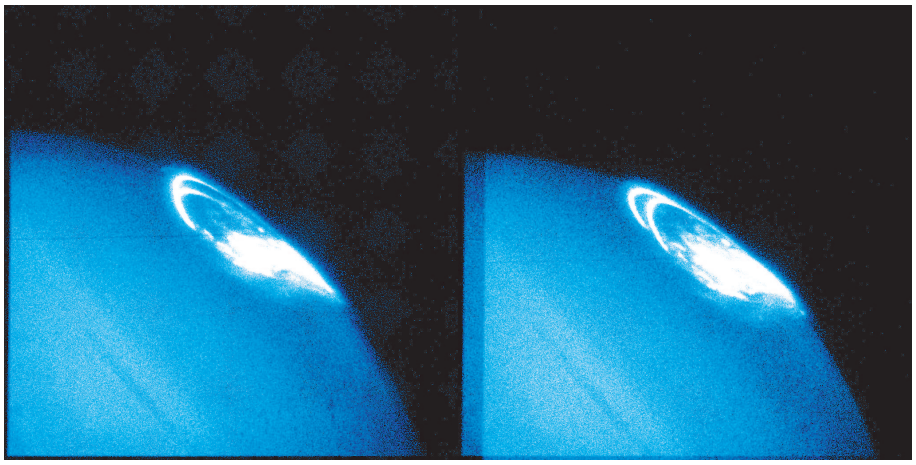

Figure 2.2: (left) Superposition of two exposures acquired during the same orbit 20 minutes apart. The two planetary disks are not aligned. (right) Superposition of the same two exposures, but shifted according to the routine results. The limbs are now perfectly aligned.

background population and the disk population so that the brightness threshold can be set to the value corresponding to the first minimum of the histogram. On unfiltered images, the situation can be more complex, especially for STIS Clear images. On the geometrically corrected images, the first population of points corresponds to the border points that do not belong to the raw image (see Figure 2.3). Their brightness has simply been set to zero in the pipeline. The second population belongs to the background points affected by $Ly-\alpha$ geocoronal emissions. The mean brightness of this population can be significantly different from zero so that a first minimum can appear on the histogram. The third population of points corresponds to the disk and auroral emissions. In this case, the second minimum threshold is considered instead of the first. At the end of this step, the threshold value is used by the procedure to discriminate roughly the points belonging to the disk from the others. The procedure then checks which corners are inside the disk and which are outside.

2.6.3 First guess of the planetary center

Given the position of the disk relative to the corners, the image is rotated in order to place the center of the disk in the lower left corner. If the disk fills two corners, the image is rotated so that the center is located on the left side. Knowing the

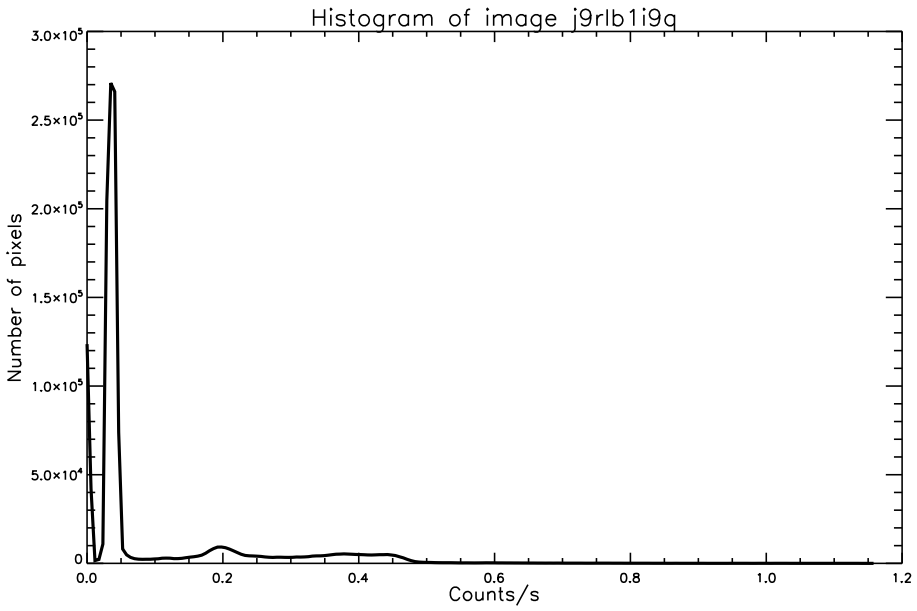

Figure 2.3: Histogram of the pixel values for a F115LP ACS image. The first peak at 0 count/s corresponds to the border points. the second maximum corresponds to the background points. The rest of the points originates from the planetary disk and the brighter points are from the aurora. In this case, the threshold is defined as the second minimum.

number of corners included into the disk, another routine locates two points at the edge of the disk taking the illumination of the limb into account. A different criterion is used for the sunlit or the dark side of the planet. At this point of the procedure, we know the quadrant in which the planet is located on the image and the approximate position of two points on the limb. A contour ellipse fitting routine based on ephemeris provides then a good first guess for the planetary center.

2.6.4 Masking the aurora

This rather accurate positioning of the center enables us to localize realistically and effectively the polar area on the images. Points in this area should be discarded from the limb scan because they are affected by high altitude auroral emissions. If a too optimistic criterion is considered, then the auroral emissions will dramatically damage the limb determination. On the other hand, if a too careful criterion is applied, then, the portion of the limb taken into account will be so restricted that no accurate limb fitting can be achieved. This is the reason why the first guess step is so important. Since the most equatorward emissions come from the Io footprint and tail, the auroral zone limit is defined 4° equatorward from the Io reference contour from *Grodent et al.* (2003a). This area enables us to build a mask of points to be discarded for the limb detection.

2.6.5 Scanning the limb

With the possibly misleading points due to auroral emissions eliminated, we can refine the determination of the limb position. The next step consists in scanning the disk boundary as approximated by the first guess ellipse in order to accurately find the location of the limb. The limb point is defined as the inflection point of the radial profile (*Vincent et al.*, 2000). Every degree starting from the bottom of the rotated images, a corresponding point from the first guess ellipse is localized and the tangent to the ellipse at this point is computed. The image is then rotated around this point in order to align the tangent line to the Y axis. The procedure selects a 240×70 pixels rectangle centered on the rotation center. The rectangle is then re-binned into a 240 points profile (see Figure 2.4). Applying the two step strategy, a two part function is first fitted to the profile for a rough determination of the brightness decrease. The first part consists in a 2nd degree polynomial which

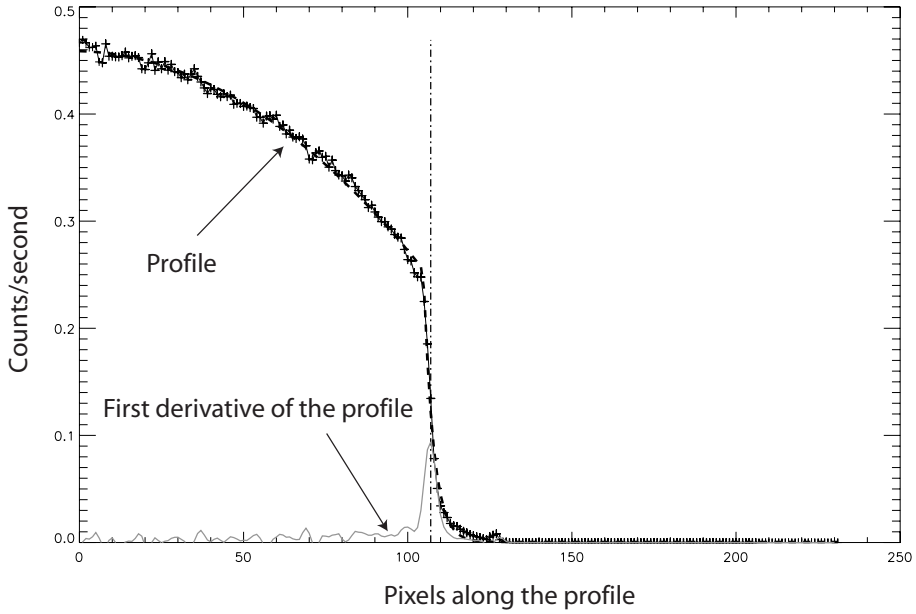

Figure 2.4: Typical limb profile for ACS data. The "+" symbols represent the actual profile. The dashed line is the polynomial-exponential fitting curve. The grey plain line represents the first derivative of the actual profile. The two step procedure, i.e. first fitting a curve and the then searching the inflection point in a restricted area, is particularly helpful for low signal to noise STIS data. The vertical dot-dashed line marks the position of the limb point.

models the behavior of the inside of the disk along a normal scan[15]. The second side of the curve is a decreasing exponential that models the transition from the disk to the background brightness. The second step consists in locating the inflection point of the profile in a restricted set of points in the part corresponding to the decreasing exponential. Finally, the locus of the inflection points is fitted with an ellipse in order to compute the coordinates of the center.

2.6.6 Deducing the orientation from the Jovian atmospheric band structure

The processing of Saturn ACS observations aquired in 2007 highlighted a systematic 0.7° error of the orientation angle when fitting synthetic rings to the image rings. Unfortunately, no ring system is visible on Jupiter HST FUV images. Neverthe-

[15]Since the orientation of the profile is perpendicular to the tangent to the ellipse, the scan is not exactly radial but normal to the limb. This is more accurate since the Jovian disk is an ellipsoid.

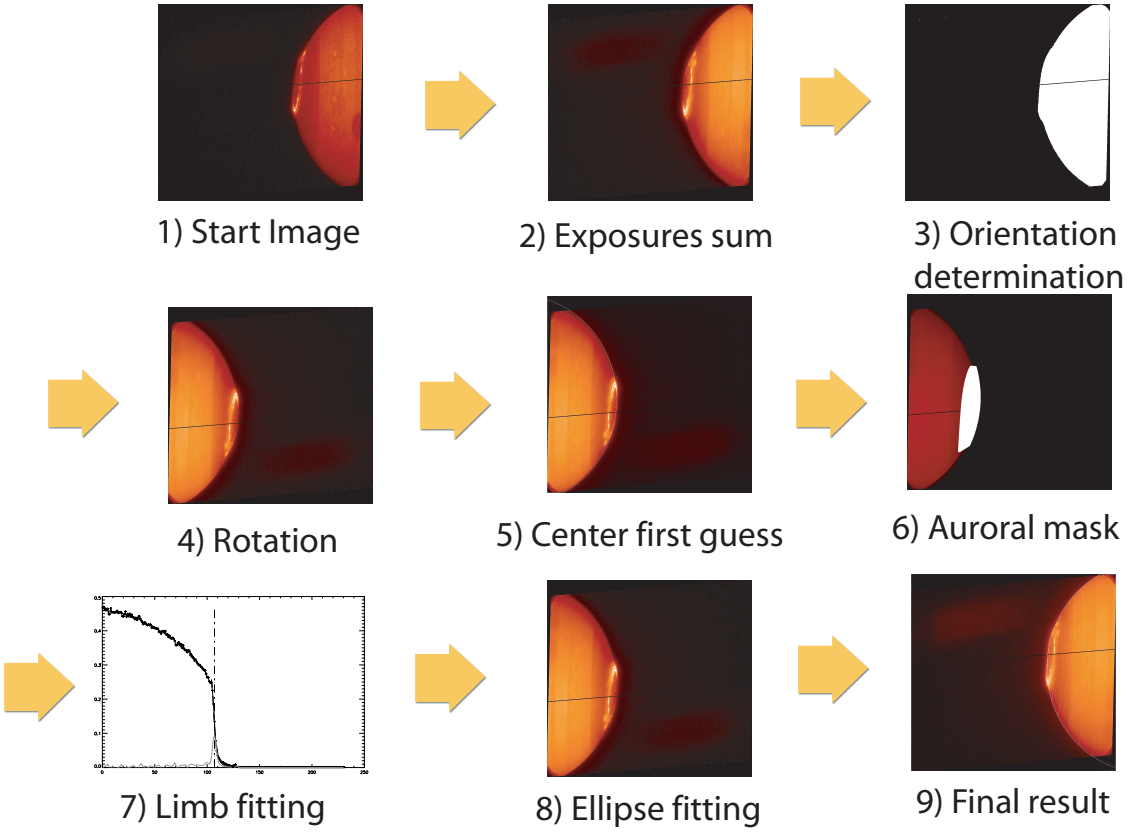

Figure 2.5: Summary of the limb fitting method.

less, the band structure of Jupiter also appears on the UV images[16] (*Vincent et al.*, 2000), even if the contrast between bands is fainter in the UV[17] than in the visible wavelengths. A band fitting procedure has been built in order to detect and measure a potential correction angle for the planetary orientation. In the southern hemisphere, the relatively sharp transition between the polar dark region and the first bright band has been used as a reference. Starting from the angle provided by ephemeris and telescope data, the algorithm projects the region of interest into the longitude-latitude space. The procedure then scans longitudinally the region and detects the maximum of the light curve slope along the meridian lines. These points are fitted linearly and the edges of the best fit line are projected into the image space. These points are then used in order to compute the correction angle directly into the original image. In order to assess and improve the accuracy of the method, a series of test angles are added to the unknown correction angle. If the procedure is efficient, it should be able to detect and measure these additional forced angles. Test angles from +1° to -1° with 0.2° steps have been used. Consequently, the value of the measured correction angle minus the test angle provides another estimation of the actual correction angle. Since the method is not perfect, some fluctuations of the measured correction angle as a function of the test angles remain (see Figure 2.6). Accordingly, the RMS departure of these fluctuations is an estimate of the intrinsic sensitivity of the method on each image and is on the order of 0.1°. The routine selects the mean value of the measured angles minus the test angles.

This procedure has only been tested on images from the 10862 program. In this image set, the mean correction angle is approximately 0.8° clockwise with an RMS deviation around 0.3° (Figure 2.7). The difference with the previous numbers is that here we evaluate the distribution of the measured values over the complete sample instead of the sensitivity on a unique image. These values are quasi-identical for both filters. No evolution has been found between the correction angle and the Day Of the Year (DOY). The deviation or the mean correction angle does not appear to be related to the CML. The root cause of the observed tilt can hardly be attributed to the guide stars inaccuracy because the angle would then be randomly distributed (the guide stars are not identical for each orbit). Inspections of set of images coming

[16]UV WFPC2 observations showed that the bright band correspond to subsidence areas while dark zones correspond to upwellings, contrary to the visible bands.

[17]The contrast between the bands , i. e. $I_d/I_b - 1$ where I_b and I_d are the brightest and the darkest portions of the bands, measured with the F160W filter on WFPC2 lies between 10 and 15% (*Vincent et al.*, 2000).

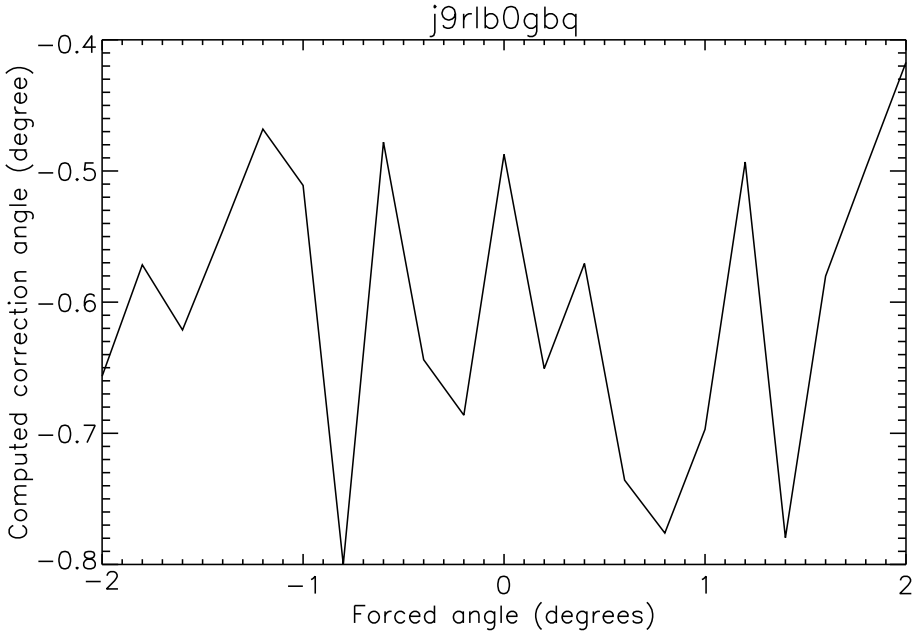

Figure 2.6: Measurement of the correction angle when different arbitrary test angles are introduced and then subtracted from the measurement. The test angles on this plot range from -2° to 2° but this range is reduced from -1° to 1° in the actual routine for computation time reasons. The RMS departure is on the order of 0.1°.

from successive orbits tend to indicate that a part of the departure from the norm could be attributed to intrinsic irregularities of the transition region between two bands. These irregularities are not surprising on these red-leak affected UV images since they are clearly noticeable on visible images (Figure 2.8).

As far as the northern hemisphere is concerned, the limit between the dark polar region and the first bright band is too blurred and cannot be used to detect the orientation angle. Several attempts to fit the maximum of the first bright band have been made, as well as attempts to fit the minimum of the first dark band. The latter provides slightly better results, but only when this band is well visible, that is when the bands are more or less parallel to a border of the image and when this dark band is not too close to the left border because of flat-fielding problems in this area (Figure 2.9). It is nevertheless obvious that none of these methods does provide a reliable estimate of the correction angle. The reason is that the contrast between the bands, their sharpness and their width vary with time and with longitude. This is also not surprising since these variations of the band structures are also obvious on visible images.

In conclusion and in agreement with Saturn observations acquired in 2007, a systematic correction of $0.7°$ to the orientation angle has been applied to every image, either North or South. New geometric correction coefficients have since been released so that the Saturn images acquired and processed since 2008 do no longer suffer from this orientation problem. Comparing the orientation angles indicated in the headers of the raw and rectified images, we see that the angular difference is $\sim 0.6°$. This number is so close from the one deduced from our previous measurements that the complete re-processing of the complete database was found unnecessary.

2.7 The Saturn observation catalog

We have seen above that Saturn images are often used as references when assessing image processing techniques for Jupiter. Indeed, Saturn is another usual planetary target for HST UV instruments. 1563 images have been acquired since 1997 with the WFPC2, STIS and ACS cameras. These observations used exactly the same instruments and the same set of filters as Jupiter images, so that they are processed in the same way. Consequently, we constructed a similar catalog for Saturn observations. This catalog includes observation campaigns 6854 (Trauger), 8158 (Prangé), 8117 (Trauger), 10083 (Clarke), 10862 (Clarke), 11566 (Nichols) and 11984 (Nichols).

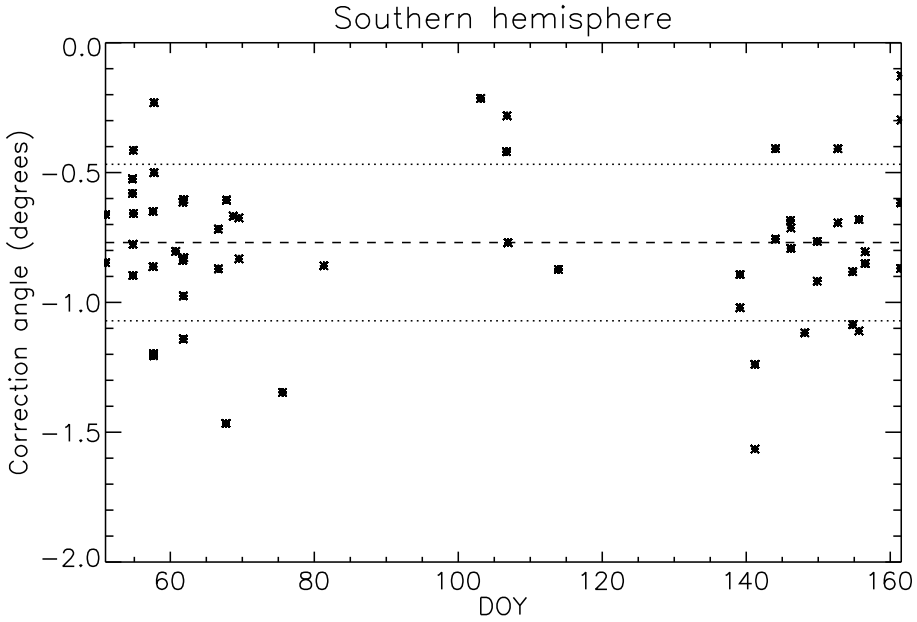

Figure 2.7: Correction angles determined from the orientation of the sharp transition region between the dark polar region and the first bright band for the southern hemisphere. The mean value of this correction is -0.77° (counter-clock wise) and is represented by the dashed line. The root mean square (RMS) deviation from this mean value is 0.3° and is represented by the dotted lines. From this plot we can see no obvious relationship between the correction angle and the Day Of the Year (DOY).

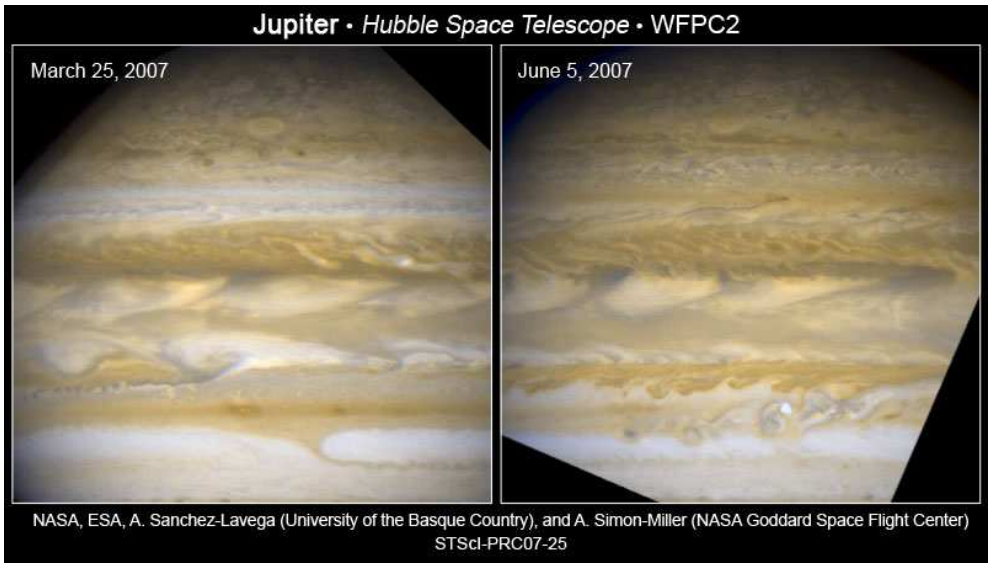

Figure 2.8: Recent WFPC2 images of the Jovian bands in the visible wavelength. It is clearly noticeable that the band contrast is changing with time and that they have sometimes irregular shapes.

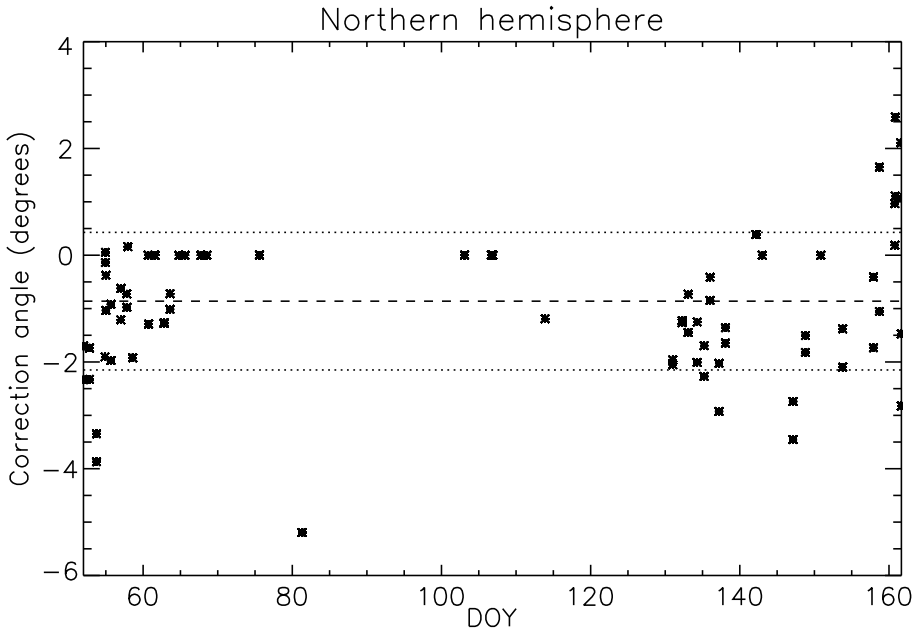

Figure 2.9: Correction angles determined from the orientation of the maximum of the first bright band for the northern hemisphere. The mean value of this correction is -0.86° and is represented by the dashed line. The root mean square deviation from this mean value is 1.3°. According to the scatter of the points on this plot, the results from this method cannot be considered as reliable.

The only differences are the center determination method and the satellite parameters. As mentioned above, Saturn's planetary centers are computed with a ring fitting method developed by Adem Saglam. Catalog fields related to Io, Europa, Ganymede and Callisto have been replaced by equivalent ephemeris parameters for Titan, Enceladus, Dione and Rhea.

2.8 Removing the planetary disk contribution

The planetary disks on STIS ans ACS images mainly originate from reflected sunlight on the planet. A classical method to model these emissions consist in modeling its variations with a generalized Minnaert function (e.g. *Vincent et al.*, 2000):

$$\ln(I\mu) = A + B\ln(\mu\mu_0) + C\ln(\mu\mu_0)^2 + D\ln(\mu\mu_0)^3$$

where I is the observed intensity, μ is the cosine of the observation zenith angle[18] and μ_0 is cosine of the solar zenith angle. This formula is an empirical function initially designed for modeling solar light scattering on the moon and has no particular physical meaning in our case. A careful analysis of the relationship between $\ln(\mu\mu_0)$ and $\ln(I\mu)$ on actual images for a given 1° wide latitude band on Jupiter shows that points on the sunlit side and points on the terminator side of the planet form two different populations (Figure 2.10). Hence, when we consider each population individually, the data points can be fitted with a linear law without the need of higher order terms. The fact that the fitting coefficients differs from the lit side to the terminator side is relatively problematic because it means that the set of coefficients should be re-considered when the angle between the Earth and the Sun as seen from Jupiter changes. For example, the Sun-Earth angle was close to 10° during the first part of the 10862 campaign while is was much closer to 0° degrees during the second one. Figure 2.11 shows an example of the A and B coefficients computed from two images acquired with the F165LP filter for each part of the campaign. When the Sun-Earth angle is close to 0° (dashed line), the behaviors on the lit and the terminator sides are similar, as expected. Similarly, they significantly differ when the absolute value of the angle increases.

The background planetary disks are built by fitting Minnaert coefficients to im-

[18]The observation zenith angle is the angle between the normal to the surface and the observer direction.

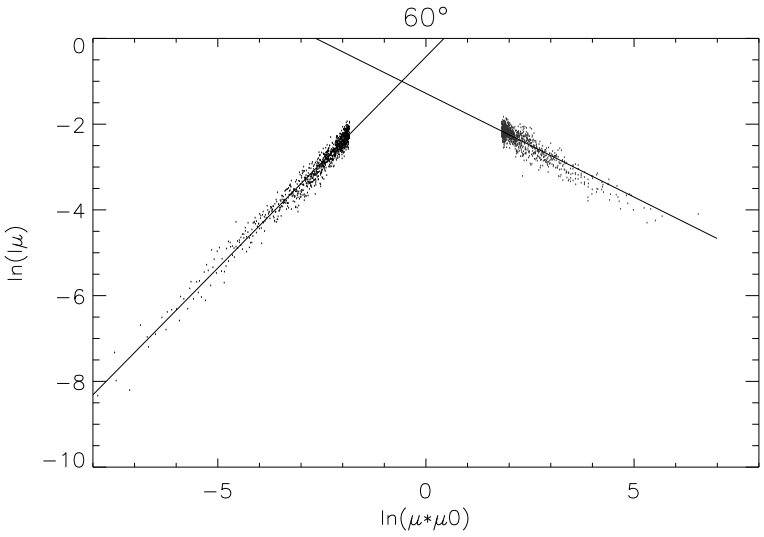

Figure 2.10: Example of the evolution of $\ln(I\mu)$ as a function of $\ln(\mu\mu_0)$. The data points with negative abscissae correspond to the lit side of the planet while points with positive abscissas correspond to the dark side (the sign of their abscissae are artificially inverted). The two sets of points have distinct behaviors which can be separately fitted with a linear law.

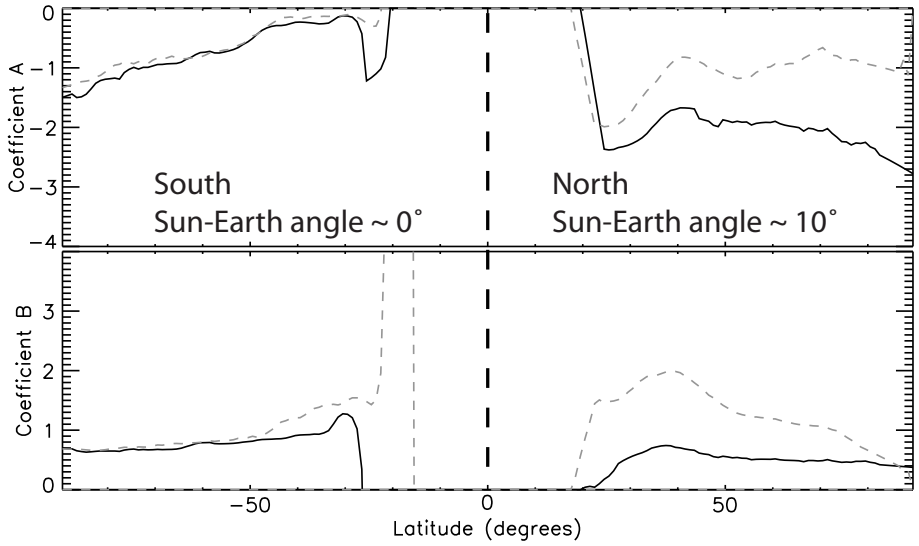

Figure 2.11: Evolution of the A and B parameters as a function of the band latitude for a F165LP filter image. This filter samples longer wavelength than the ones we usually use and is therefore less sensitive to the auroral emissions. The curves on the left part of the image correspond to a configuration where the Sun-Jupiter angle was close to 0° and no large differences are seen between the sunlit (solid line) and the terminator side (dashed line). The curves on the left part of the plot correspond to a configuration where the Sun-Jupiter angle was close to 10°. In this case, the A and B parameters are different for the sunlit and the terminator side.

ages void of any auroral emissions. These "disk only" images are constructed from a combination of real images. The idea is to assemble images where the aurora is located in a different sectors of the planet, through the use of masks hiding the auroral emissions. For example, we can use an image where the auroral emission is concentrated on the dusk side and another where the aurora is concentrated on the dawn side. For each of them, we manually define a mask hiding the auroral emissions. Then we re-size and rotate the second image so that the planetary centers and the orientations coincide (Figure 2.12). Afterwards, we can assemble the "disk only" image: when the brightness is available on both images, we consider the mean intensity, when only one brightness is available because its counterpart is hidden by the auroral mask, we consider this intensity and we discard points where no information is available. This assembled image can then be used to fit the Minnaert coefficients. Since the band intensity varies with latitude, we compute 4 coefficients per 1° wide band: two for the lit side and two for the terminator side. Very high latitude coefficients are usually missing because of the lack of data points. Low latitudes are also usually undersampled or affected by an unreliable flat field correction on the image borders. However, the typical IFP latitudes are always well covered and thus the disk can be removed accurately in these regions.

Based on the particular orientation of each image, a synthetic background planetary disk is generated for each image of the catalog. This disk can then be simply removed from the original image in order to isolate the auroral emissions.

2.9 Epilogue: contributions to the study of Jupiter's and Saturn's aurorae

The catalogs and the data processing techniques discussed above were necessary to study the satellite footprints and Io's auroral signature in particular. However, these techniques have also been used for studies of the giant planet aurorae unrelated to the Io footprint. A detailed description of these results is out of the scope of present thesis, but they nevertheless deserve to be quickly mentioned here.

The availability of a common and standardized catalog for all Jovian UV images, whatever the instrument or whatever the observation campaign, makes comparisons from one dataset to another easier. For example, *Grodent et al.* (2008b) showed that the location of the main auroral emissions as well as the location of the footpath of

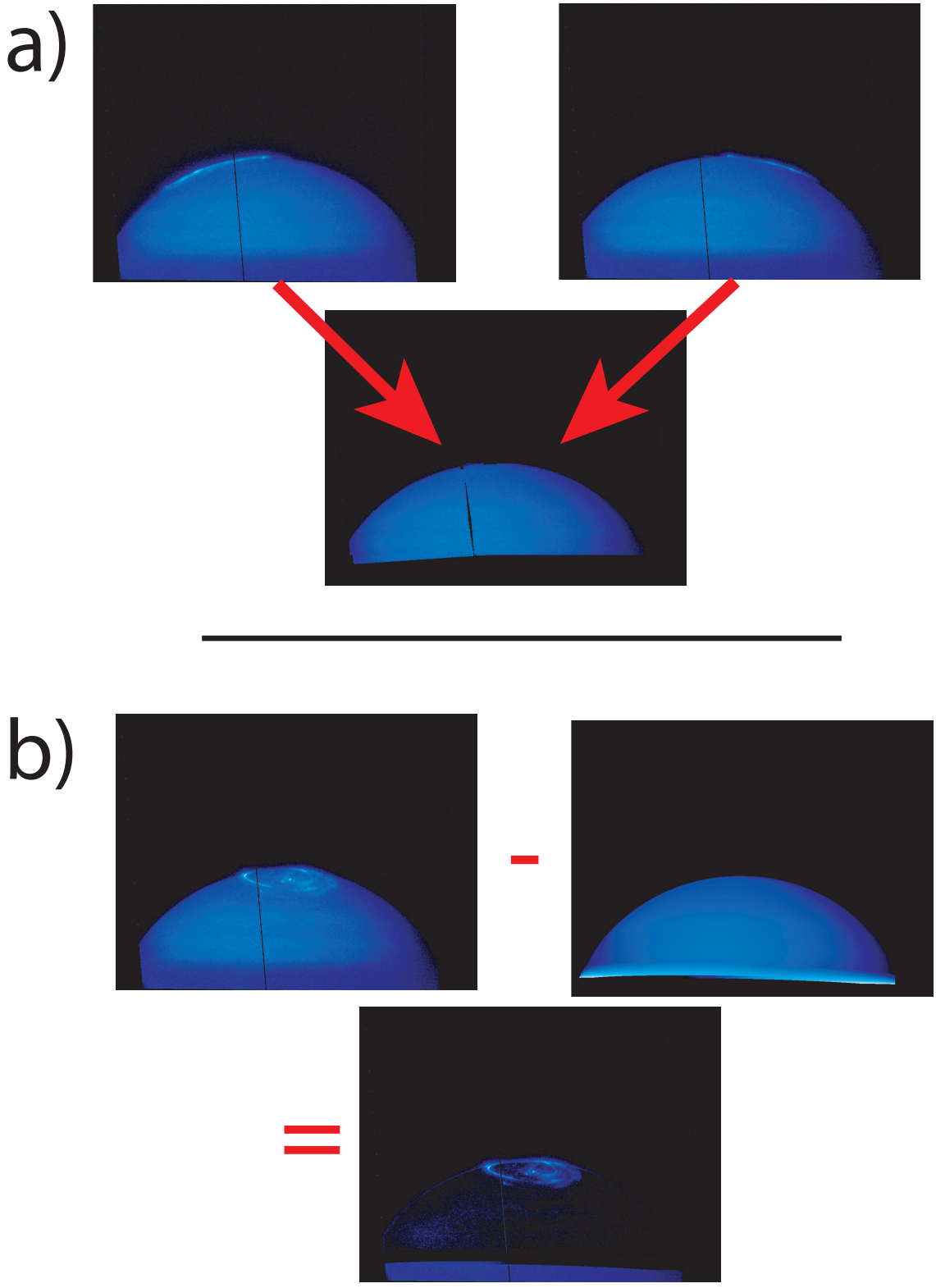

Figure 2.12: In order to determine the Minnaert coefficients, for given epoch and a given filter, we combine two or more images into an assembled image void of auroral emissions (a). These coefficients are then used to generate a synthetic background disk for each image (b).

Ganymede were varying by superimposing polar projection of the auroral emissions from different epoch (Figure 2.13). They showed that variations of the ring current characteristics could explain these changes.

Moreover, the accurate and systematic determination of the planetary center on Jupiter considerably facilitated the localization of the different features on Jupiter and the variation of these positions. Once the planetary centers and orientations are known, polar projections of the auroral features can be automatically computed. The limb fitting procedure presented here made the early production of the complete set of polar projections related to the 10862 campaign possible only a few weeks after the end of the observation campaign, significantly accelerating the production of scientific results. *Radioti et al.* (2008a) used these polar maps to produce statistics of the position of the discontinuity in the brightness of the main oval. This discontinuity has been associated to a reversal of the field aligned currents related to the breakdown of corotation of the magnetospheric plasma. In addition, the same early polar projections enabled the statistical analysis of the polar dawn spots (*Radioti et al.*, 2008b). The polar dawn spots are localized features present in the polar region (i.e. poleward of main auroral oval). Their re-occurrence period of 2 to 3 days strongly suggests that they are associated with internally driven magnetic reconnection in the Jovian magnetotail.

Other interesting auroral features on Jupiter are the faint diffuse emissions observed equatorward of the main oval. A comparison between simultaneous measurements made by HST and the Galileo spacecraft suggests that these diffuse emissions could be linked to the pitch angle distribution boundary(*Radioti et al.*, 2009b). This boundary corresponds to a transition region located in the middle magnetosphere between 10 and 17 R_j and where the distribution of the electron pitch angle changes from pancake to bi-directional.

Finally, the image processing routines and the Saturn catalog have been used to study transient features in the Kronian aurorae (*Radioti et al.*, 2009a). These time-varying emissions are though to be linked to energetic particle injections, similar to the injections thought to trigger the "plasma blob" emissions on Jupiter.

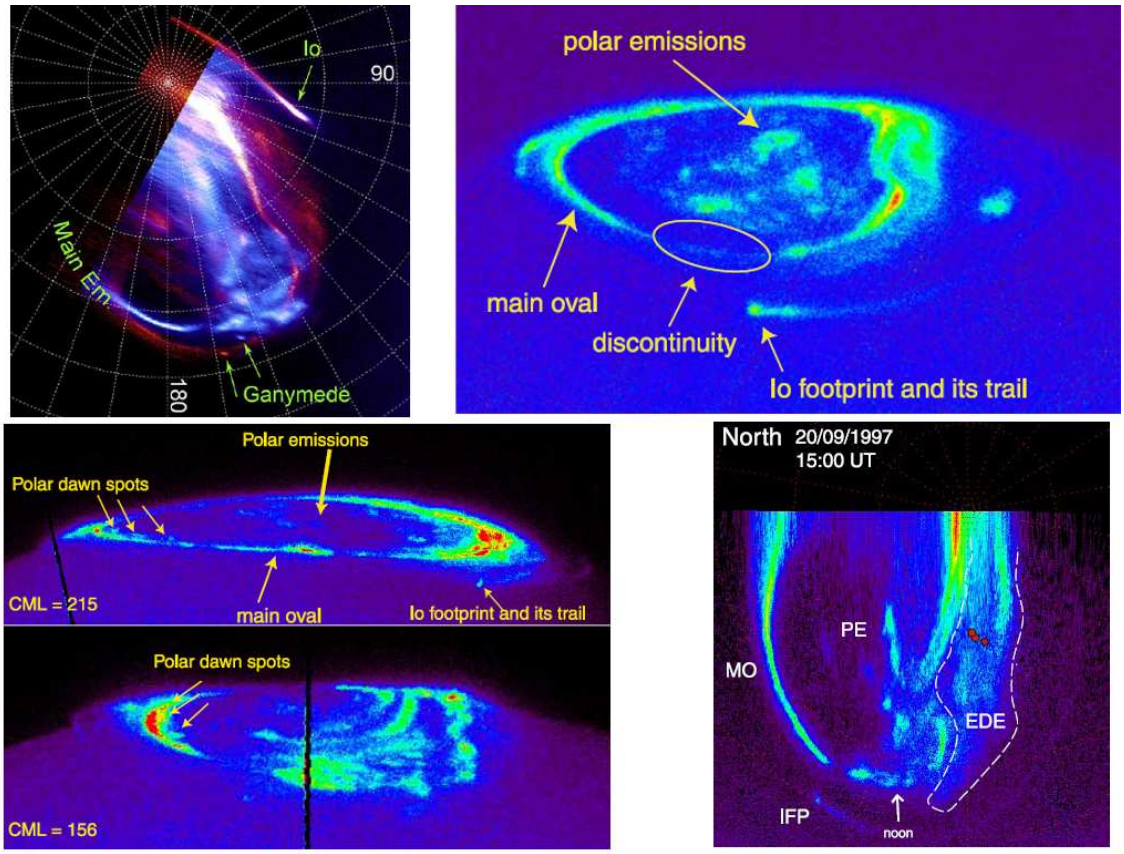

Figure 2.13: (top left) Superposition of two polar projections of the Jovian northern aurora. The red one was acquired in December 2000 with the STIS instrument while the blue one was acquired in April 2005 with the ACS camera. (from *Grodent et al.* 2008b) (top right) Image of the northern aurora highlighting the discontinuity of the main oval. (from *Radioti et al.* 2008a) (bottom left) Examples of polar dawn spots. These spots are though to be related to internally driven reconnections in the Jovian magnetosphere. (from *Radioti et al.* 2008b) (bottom right) Polar projection of a STIS northern aurora image acquired the same day at the time Galileo crossed of the pitch angle distribution (PAD) boundary. The dashed lines isolate the equatorward diffuse emissions (EDE). The red circles represent the projected locations where Galileo detected PDA boundaries and the red diamond represent the expected Ganymede footprint position when Ganymede's System III longitude is 40°. (from *Radioti et al.* 2009b)